Field-Effect Transistor with a Plasmonic Fiber Optic Gate Electrode as a Multivariable Biosensor Device

Roger Hasler,* Ciril Reiner-Rozman, Stefan Fossati, Patrik Aspermair, Jakub Dostalek, Seungho Lee, Maria Ibáñez, Johannes Bintinger, and Wolfgang Knoll*

ACCESS | Metrics & More | Article Recommendations | Supporting Information

ABSTRACT: A novel multivariable system, combining a transistor with fiber optic-based surface plasmon resonance spectroscopy with the gate electrode simultaneously acting as the fiber optic sensor surface, is reported. The dual-mode sensor allows for discrimination of mass and charge contributions for binding assays on the same sensor surface. Furthermore, we optimize the sensor geometry by investigating the influence of the fiber area to transistor channel area ratio and distance. We show that larger fiber optic tip diameters are favorable for electronic and optical signals and demonstrate the reversibility of plasmon resonance wavelength shifts after electric field application. As a proof of principle, a layer-by-layer assembly of polyelectrolytes is performed to benchmark the system against multivariable sensing platforms with planar surface plasmon resonance configurations. Furthermore, the biosensing performance is assessed using a thrombin binding assay with surface-immobilized aptamers as receptors, allowing for the detection of medically relevant thrombin concentrations.

KEYWORDS: electrolyte-gated field-effect transistor (EG-FET), surface plasmon resonance (SPR), layer-by-layer (LBL) assemblies, surface investigation, multivariant sensing, fiber optics, sensor geometry
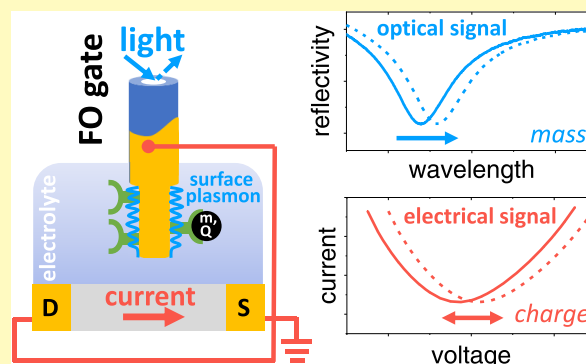
Recent global events have demonstrated the importance of portable biosensors as point-of-care devices. Electrolyte-gated field-effect transistors (EG-FET) are excellent candidates for affinity biosensors, providing functionalization with a biorecognition unit, for instance, on the gate electrode surface.[1] Binding events manifest themselves as changes in the source–drain current I_{DS} and the underlying mechanisms have been extensively studied over the last few years.[2−4] However, to validate the sensor response, additional insights are required, preferably using a multivariable readout of the sensor surface, e.g., combining a field-effect transistor (FET) with a quartz crystal microbalance,[5] surface acoustic wave sensors,[6] fluorescence,[7] electrochemistry, and other techniques.[8] These sensor fusion concepts provide additional insights into the (bio-)surface processes, for instance the mass uptake, thus grant a deeper understanding and optimization potential. It has been shown that multivariable readout facilitates an ubiquitous characterization of surface events by monitoring independent variables.[9] In previous work, we have demonstrated the advantages of simultaneous measurements on the same surface using plasmonic and electronic sensors to monitor mass and charge uptake.[10] Compared to the abovementioned dual-mode sensor systems, this provides an optical and electrical response using a label-free detection without the need for an additional reference electrode.

Alternatively, such dual modality has been reported using simple and easy to fabricate plasmonic sensors based on a gold/silicon Schottky junction.[11] In this context, here, we present a novel EG-FET sensor platform using a gold-coated optical fiber that acts simultaneously as a gate electrode and substrate for surface plasmon (SP) resonance (SPR) spectroscopy. To the best of our knowledge, this sensor configuration has not been demonstrated before. In addition to the electronic readout of the FET, a binding event at the fiber gate/electrolyte interface yields an optical signal due to a local refractive index change associated with mass uptake on the surface of the fiber gate. The coupling to surface plasmons via optical fibers allows for the miniaturization of the optical components and simplifies the integration to an EG-FET sensor significantly. The device geometry is crucial for the performance of the presented sensory system due to the strong dependence of the electrical and optical readout of fiber gate electrodes on the geometrical properties.[12,13] Hence, in this
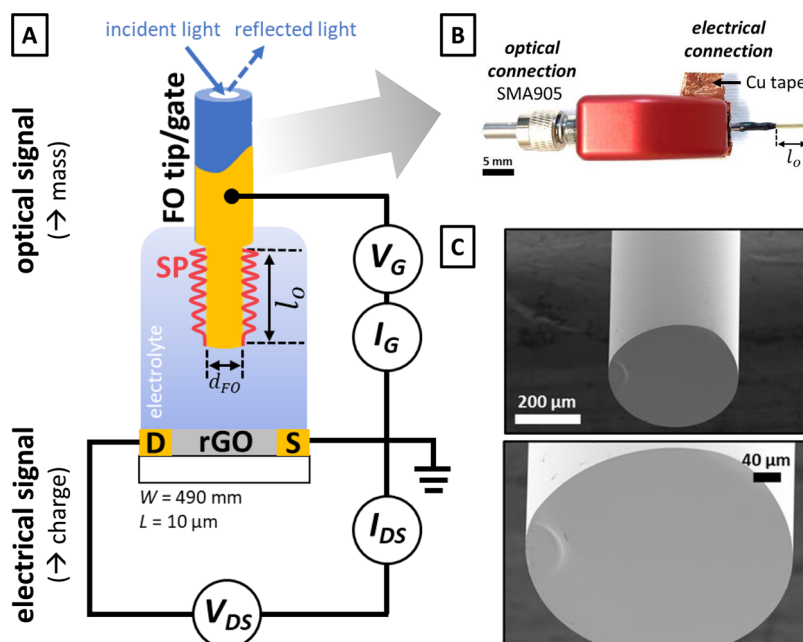
A

Figure 1. (A) Schematic representation of the presented EG-FET/FO-SPR measurement platform. The FO gate with core diameter d_{FO} consists of an SPR active zone with length l_o. (B) FO gate connection for simultaneous optical and electrical readout. (C) Scanning electron microscopy (SEM) images of the gold-coated FO tip and its cross-section.

work we optimize the presented novel system by varying optical fiber diameters and evaluate the resulting optical quality factors and electrical transfer characteristics. Furthermore, the effect of an applied gate voltage on the optical readout of such gold-coated fiber gate electrodes is investigated to ensure measurement stability while operating the optical fiber in its dual-operation mode. The combined sensor platform is validated using a layer-by-layer (LbL) assembly of oppositely charged polyelectrolyte multilayers (PEMs) on the fiber gate of a reduced graphene oxide (rGO)-based EG-FET. The LbL assembly is deposited by subsequent adhesion of positively and negatively charged polyelectrolytes and its growth is monitored. This model system was chosen as a proof of principle due to its good reproducibility and comparability to other platforms and furthermore plays a crucial role in a wide range of applications, e.g., water desalination[14] or drug delivery.[15] Furthermore, we demonstrate the bioanalytical capabilities using an aptamer-based assay for thrombin detection. In addition to monitoring and cross-validating surface binding kinetics, the presented sensing platform also allows simultaneous monitoring of surface mass and charge density variations.

■ EXPERIMENTAL SECTION

Plasmonic fiber optic (FO) probes were prepared according to previously reported procedures (also see the Supporting Information (SI)).[16] Briefly, the optical probes were constructed from TECS-clad step-index multimode optical fibers with a numerical aperture of 0.39, various core diameters (400, 600, 800, and 1000 μm, respectively), and cut to a length of approximately 7 cm. An SPR-sensitive zone was constructed at one end of the tip by removing the jacket layer with a dedicated stripping tool, followed by dissolving the polymer cladding layer with acetone. The planar cut at the end face was obtained using a fiber optic scribe with a ruby blade. FO tips were cleaned with Milli-Q grade DI-H$_2$O and isopropanol and blow dried with compressed air. Thereafter, the tips were sputter-coated homogenously with 50 nm of gold. Details of the used sputter conditions can be found in the SI (Section S2). The optimization of the Au layer thickness and its

influence on the obtained optical signal is shown in Figure S3. The two sections of the FO probes were connected using silver paint and afterward coated with liquid insulation tape (Figure S1).

According to a previously reported procedure, FETs were fabricated using commercially available substrates with interdigitated electrodes (channel width 10 μm, length 490 mm) (see the SI).[17] Graphene oxide (GO) was deposited via spin coating on the (3-aminopropyl)triethoxysilane (APTES)-functionalized substrates. The obtained GO-coated substrates were reduced with hydrazine monohydrate at 80 °C for 16 h followed by annealing at 200 °C for 2 h under vacuum.

Plasmonic fiber probes were connected to the optical part of the setup, similar to that reported by Kotlarek et al., via a commercially available bare fiber terminator (see the SI).[18] Light was guided to the tip of the plasmonic fiber probe to resonantly excite propagating surface plasmons on its outer gold surface. The gold-coated cross-section acted as a mirror to reflect light, which was coupled back to the Y-optical splitter and guided to a spectrometer. The measured spectrum of the back-reflected light beam was normalized to air measurements. The normalized reflectivity spectra were processed using dedicated LabView software.[19] These optically connected, gold-coated fiber probes were simultaneously used as gate electrodes (FO gate) in an EG-FET configuration (Figure 1A). Therefore, the FO gate was inserted in the reaction chamber, where the fabricated FETs were placed and connected to the probe station. The electrical connection of the FO gate was achieved using conductive copper tape within the bare fiber terminator to contact the gold-coated surface at the upper end of the probe (Figure 1B). By applying a sweep potential ranging from −0.5 to 0.5 V on the FO gate (with sweep rates between 0.09 and 0.25 V/s), the source–drain current vs gate voltage ($I_{DS}V_G$) transfer characteristics were recorded. For all experiments, a drain–source voltage of 50 mV was applied, corresponding to the linear regime of the drain–source voltage vs current characteristics for any given V_G (figure S16). Connected FO gate electrodes were used for combined optical and electrical sensing. Therefore, the FO gate surface was functionalized by dipping in the respective analyte solution while performing a continuous optical measurement based on tracking the resonance wavelength over time. After each functionalization and subsequent washing step, the FO gate was placed into the cavity of the reaction chamber. Five consecutive $I_{DS}V_G$ transfer curves were recorded, and after stabilization of the optical
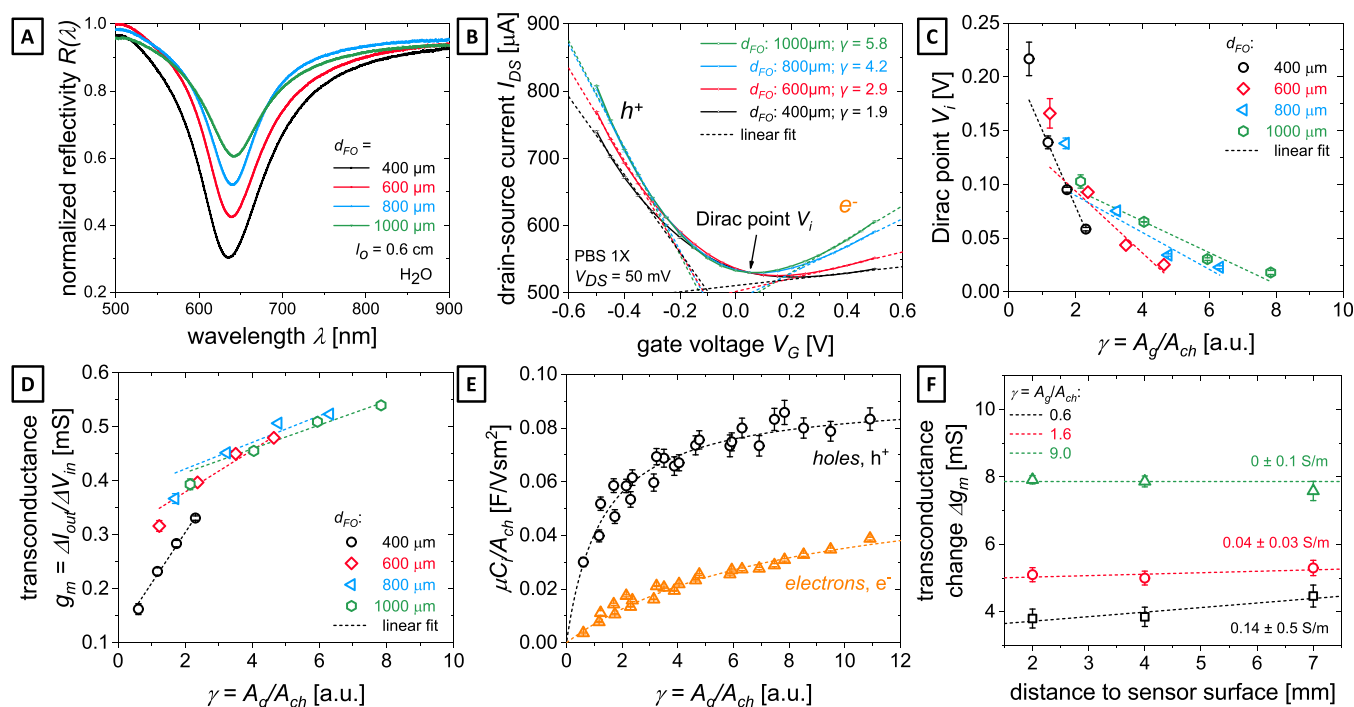
Figure 2. (A) Wavelength-dependent resonance spectra for different d_{FO} in water. (B) Averaged $I_{DS}V_G$ curves of different d_{FO} measured in PBS. h^+ and e^- indicate hole and electron mobility branches with fits of the linear regime (dashed lines). Dependence on the surface area ratio of (C) Dirac point and (D) maximum transconductance determined from $I_{DS}V_G$ curves for d_{FO} and l_{gate} ($\leq l_o$) variation. Dashed lines indicate linear fits for a given d_{FO}. (E) The correlation of the capacitance depending on the $\gamma = A_g/A_{ch}$ ratio for hole-dominated and electron-dominated sections with fits of eq 2. (F) Influence of the gate to FET surface distance on the transconductance depending on the gate to channel size ratio γ. Dashed lines indicate linear fits for a given γ.

signal, the FO gate was dipped into the next analyte solution. This procedure was repeated for each functionalization step. The exact exposure time was kept constant between dipping the modified FO gate into the reaction chamber and recording the $I_{DS}V_G$ curves. Details about the procedure applied for the two model assays are given in the SI.

RESULTS AND DISCUSSION

A dual-mode sensing platform was designed based on an EG-FET using a gold-coated FO probe as the gate electrode and the optical surface for simultaneous surface plasmon optical and electrical readout (Figure 1A). Figure 1B shows the connection of the FO gate to the optical and electrical system. A uniform gold coating of the fiber tip beyond the SPR-sensitive zone was obtained, with an average thickness of 48.5 ± 2.5 nm and a root-mean-square (RMS) surface roughness of 1.85 nm, determined via SEM and atomic force microscopy (AFM) measurements (Figures 1C and S4–S8). A planar surface on the FO gate tip has to be achieved by cutting to ensure reliability and stability of the recorded data. To control the quality of the cutting method, SEM images of the fiber tips were recorded with a stage tilt angle of 50° to the normal vector of the tip surface and are shown in Figure 1C. A smooth cut with a minor point of rupture on one edge was observed, which was deemed sufficient for application.

The electrical signal transduction is based on drain–source current (I_{DS}) modulation in the semiconducting material according to

$$I_{DS} = \frac{W}{L} C_i \mu (V_G - V_T) V_{DS} \qquad (1)$$

where W is the channel width, L is the channel length, C_i is the insulating layer capacitance, μ is the charge mobility of the semiconductor, V_T is the threshold voltage, V_G is the gate voltage, and V_{DS} is the drain–source voltage. A surface event at the gate–electrolyte interface is associated with a change of C_i and therefore results in a change of I_{DS}.[1,20,21] Depending on the type of semiconductor a depletion or accumulation mode defines the shift direction, for ambipolar materials like rGO the applied V_G enables switching between both modes.

The optical signal transduction is based on the detuning of the resonant optical excitation of propagating surface plasmons (SP) at the metal–electrolyte interface due to a local refractive index change, which can be associated with mass adsorption on the sensor surface.[22] The FO gate connection via the optical Y-splitter allows for coupling and guiding white-light to the SPR-sensitive zone l_o of the tip to resonantly excite propagating SP on its lateral gold surface.[23] As previously reported, the optical signal depends highly on the number of reflections of the light (eq S2, SI).[23] It can be seen that the coupling strength (represented as a minimum of the SPR dip in the reflectivity wavelength spectrum) is decreasing at the resonance wavelength and the SPR dip is becoming broader with increasing core diameter at a fixed l_o (Figure 2A).[24] Experimental validation was obtained by recording optical signals from FO tips with l_o = 6 mm and increasing d_{FO} from 400 to 1000 μm. These findings verify that for lower d_{FO} more pronounced reflectivity minima, as well as a broader spectral dip are obtained. The influence of the gate area A_g on the electrical signal was investigated, for a sufficient length l_o needed for a satisfactory optical signal according to eq S2. Therefore, FO gate electrodes with various diameters were dipped into a phosphate-buffered saline (PBS) electrolyte solution and $I_{DS}V_G$

curves of the FET were recorded by sweeping V_G from −0.5 to 0.5 V (Figure 2B). A significant dependency of the recorded transfer characteristics on the FO core diameter was observed. Only a few publications on EG-FETs address the influence of the geometry and the electrode surface area on the electrical signal.[12,25−27] The ratio of gate area to channel area has been identified as a crucial parameter for the observed effect.[25] The FO gate surface area was calculated by approximating a cylindrical shape with a length derived by analysis using ImageJ.[28] Since all FO gates used to study the FO gate size influence were sputtered at once, surface roughness was considered the same for all FO gate diameters. For the FET active channel, a total channel area A_{ch} = 3.1 mm^2 was calculated for the interdigitated electrode geometry and rGO surface coverage. Only the rGO-covered area forms the active part of the channel area and as previously reported, a surface coverage of 63% was a good trade-off between a high current readout showing only a minimal baseline drift.[17] Four d_{FO} with sizes of 400, 600, 800, and 1000 μm were tested, resulting in surface area ratios $\gamma = A_g/A_{ch}$ = 1.9, 2.9, 4.2, and 5.8, respectively (for a length of 6 mm). Furthermore, the dipping depth of the FO gate into the buffer solution, l_{gate}, was varied for each different d_{FO}, effectively changing γ by height variation (eq S1) to obtain closer insights into the underlying correlations (Figures S11−S15, SI). Therefore, for each measurement, the FO gate was lowered subsequently into the solution by lifting the reaction chamber on a stage with a below-millimeter precision. Evaluation was performed by two characteristic parameters of $I_{DS}V_G$ curves in PBS buffer: (i) the minimum of the transfer curve (Dirac point V_i), obtained by fitting the recorded $I_{DS}V_G$ curve via second-order polynomial fit and evaluating the minimum, and (ii) the transconductance g_m defined as the ratio of I_{DS} at $V_G = -0.5$ V and I_{DS} at V_i ($\Delta I_{out}/\Delta V_{in}$). Figure 2C,D shows the resulting EG-FET characteristics and in both cases, a significant dependence on γ can be observed. A linear correlation of γ and V_i, as well as γ and g_m were found as expected according to eq S1, with increasing slope for smaller gate surface areas. The observed enhancement of the current at a given V_G with higher γ results in a steeper slope for both, the hole (h$^+$) and electron (e$^−$) accumulation branches of the ambipolar $I_{DS}V_G$ curves. The underlying mechanism is an increase in the electrolyte/gate interfacial capacitance C_g which scales with the area.[29] No significant influence of the distance from the EG-FET channel to the FO gate on the $I_{DS}V_G$ curves was observed (Figure S15, SI). We hypothesize that the underlying mechanism, which could affect the sensor performance at different gate to channel distances is overcome by sufficiently long distances, and hence delayed ion travel times through the bulk, leading to constant charge accumulation for positive and negative gate bias inversion during the transfer characteristic recording time window.[30] Concomitant with this observation, low switching speeds, and sweep-rate-dependent $I_{DS}V_G$ curves are inherent for the presented system.[31] The applied potential window also determines the magnitude of influence of the gate distance on the FET performance and in contrast to other studies (where poly(3-hexylthiophene-2,5-diyl) (P3HT)-based organic field-effect transistors (OFETs) were used),[32] we report that the herein presented configuration with the tested A_g/A_{ch} ratios, can be operated in a potential window spanning at least from −0.5 to 0.5 V (Figure S11, SI). For application in biosensing, the potential window is highly suitable as the applied voltages ($|V_G|$, $|V_{DS}|$) are below 1 V. This prevents electrolysis of the

electrolyte solution and leads to good operational flexibility under physiologically relevant conditions. Low switching times are not a significant limitation for the intended application, as single $I_{DS}V_G$ measurements based on a capacitive sensing concept are used for observation of binding events on the active surface (FO gate). The slope of the recorded transfer curves was determined and used to derive the product of mobility μ and capacitance C_i of the system according to a previously reported method.[20] Since the same FET channel was used for comparisons with different gate areas, the mobility is considered a material constant therein. The product thereof, normalized by the channel area A_{ch}, $\mu C_i/A_{ch}$, was correlated with γ to show the change in capacitance for an increase of the gate electrode area (Figure 2E). For high γ (large gate areas), the capacitance at the channel/electrolyte interface dominates ($C_{ch} \ll C_g$) leading to a constant $\mu C_i/A_{ch}$ ratio. However, for low γ (small gate areas), the capacitance at the gate/electrolyte interface dominates ($C_{ch} \gg C_g$) and the ratio $\mu C_i/A_{ch}$ falls off rapidly with decreasing γ. The obtained data were fitted to the relationship reported by O'Suilleabhain et al. adapted to the area ratio instead of volume[26]

$$\frac{\mu C_i}{A_{ch}} = \frac{\mu C_{ch}}{1 + \left(\frac{A_{ch}}{A_g}\right)\left(\frac{C_{ch}}{C_g}\right)}$$

(2)

The resulting fits for electrons and holes are shown in Figure 2E and the corresponding R^2 coefficients of determination were 0.94 for both. The influence of the FO gate distance to the FET channel was further investigated by performing measurements of the source−drain voltage vs source−drain current ($I_{DS}V_{DS}$) for different applied V_G. These investigations were performed with three different FO gate diameters and variable dipping depths (distances) of the electrode while scanning the $I_{DS}V_{DS}$ curves with variations of V_G in steps of 100 mV from 0.1 to −0.5 V (Figure S16, SI). For each set of FO diameter and dipping length, the influence of the gate voltage was evaluated by subtracting the minimum I_{DS} value (at V_G = 0.1 V) from the maximum I_{DS} value (at V_G = −0.5 V). By normalization of the factor resulting from this subtraction to a change of 1 V, we show the change in transconductance, Δg_m, as a function of the exposed FO gate area. The results are shown in Figure 2F and the influence of the dipping depth (x-axis, distance from the sensor surface) on the transconductance change decreases with increasing FO diameter (γ ratio, linear fits). For FO gate diameters of 1 mm, the FO gate distance to the sensor surface showed almost no influence on the transconductance (slope close to zero, green line), while for FO gates with lower diameters a significant slope (black line) is observed for the investigated distances from 2 to 7 mm. Furthermore, the influence of the gate area on the Faradaic currents and their proportion on the sensor signal was investigated. By varying the scan rate while sweeping V_G and monitoring the leakage current I_G for different γ ratios, we observe a power-law relationship which in turn was used to deconvolute Coulombic and Faradaic contributions. A detailed analysis is shown in Figure S17, SI. The results show that higher ratios γ, lead to an increase in faradaic currents and represent a drawback with increasing d_{FO}. Regardless, passivation of the sensor surface is expected to overcome this limitation. The dependence of the electrical signal on A_g indicates that a defined l_{gate} is crucial for device performance. To confine the optical and electrical probing area to the same
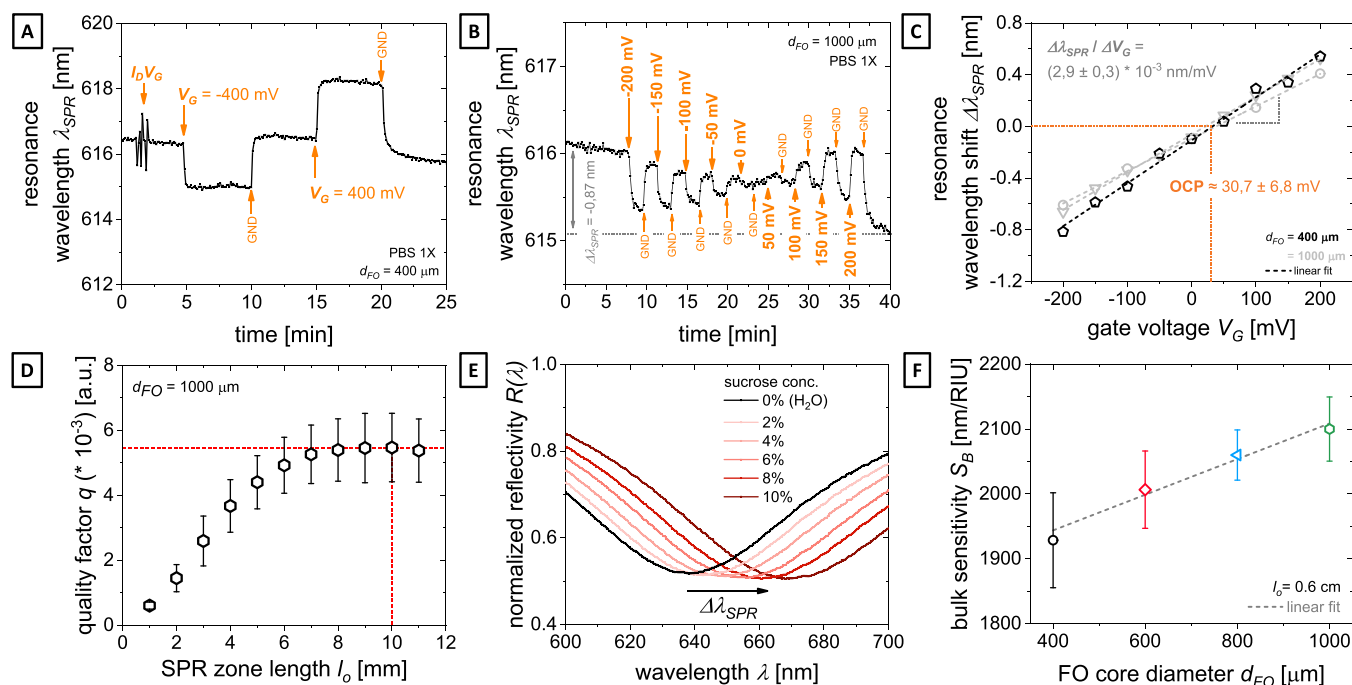
Figure 3. (A) Influence of $I_{DS}V_G$ recording on the optical signal (V_G = −0.5 to 0.5 V, sweep rate = 0.09 V/s). The application of a constant V_G of −0.4 and 0.4 V causes a reversible and constant offset of the resonance wavelength. (B) Step-wise switching of V_G from −0.2 to 0.2 V with 50 mV step size. (C) Linear correlation of the obtained resonance wavelength shifts depending on V_G. (D) Dependence of the q factor on the SPR zone length resulting in an optimal l_o of 10 mm for 1000 μm FO probes (indicated by red dashed lines). (E) Change of the spectral position of the resonance dip, $\Delta\lambda_{SPR}$, upon exposure to sucrose solutions. (F) The linear increase in bulk sensitivity of the optical signal with an increase in the core diameter for a given l_o = 0.6 cm.

spot on the fiber ($l_{gate} = l_o$) with a well-defined length, the FO gate was dipped into the electrolyte until the liquid level reached the heat shrink tube-coated section of the FO tip.

Furthermore, the influence of the applied V_G on the FO tips on the obtained optical signal was investigated. Changing the electrochemical potential alters the optical properties of a metal−electrolyte interface. Previously, this effect was attributed to voltage-induced changes of the free electron density in the surface layer of Au leading to a modification of the electron density-dependent dielectric constant of gold and consequently to a shift of the plasmonic resonance dip.[33] However, more recent studies show that the applied potential influences the optical signal also due to the formation of ionic complexes on the metal surface by tuning the chemical equilibrium, therefore, modulating the amount of adsorbed ionic species.[34,35] Applied potentials manifest themselves as shifts of the resonance wavelength in the optical sensor response. To demonstrate the reversibility of this effect, the optical signal was recorded with a bare gold surface in PBS, while different V_G biases were applied on the FO gate for a period of 25 min and the resulting kinetic curve of the SPR is shown in Figure 3A. This experiment demonstrates good reversibility of the optical signal for applied V_G biases with regeneration times of the resonance wavelength below 10 s after switching V_G to ground. However, electric field coupling to the plasmonic signal becomes apparent as a disturbance in the optical signal when sweeping V_G from −0.5 to 0.5 V to record $I_{DS}V_G$ curves. The impact thereof depends on both, the integration time of the spectrometer as well as the scan rate with which the gate voltage is swept. For a fast V_G scan rate (0.1 V/s) and the total optical integration time of ≈1.5 s only a minor impact on the optical response was observed. However,

applying a constant gate voltage leads to a substantial offset of the optical response, with a negative potential leading to a blue shift and a positive potential to a red shift of the resonance wavelength. In Figure 3B the SPR kinetics are recorded while applying a step function with 50 mV steps and intermediately switching back to the ground with step duration adjusted to ensure optical signal stabilization for each step. Figure 3C shows the resulting dependency of the SPR signal on the applied potential steps. A clear linear correlation is found and therein the V_G corresponding to no shift in the SPR signal can be obtained, which we interpret as an indirect determination of the open circuit potential (OCP) found at 30 ± 7 mV. Even though the optical readout is influenced by an applied V_G, it is possible to deploy plasmonic FO tips as gate electrodes and utilize both sensing channels for simultaneous sensing. In practical application, the electrical signal is recorded by sweeping the gate voltage when the optical signal is stabilized in the electrolyte solution with minor impact and the next analytical step is carried out after restabilization of the optical signal. In the second mode of operation, a constant V_G is applied and leads to a constant offset of the resonance wavelength, but the information in the optical signal is still preserved since the optical sensing principle relies on relative shifts only. As reported in the literature, an irreversible blue shift of the resonance wavelength upon prolonged application of potential can be observed, which is attributed to a potential-induced grain growth of the in-vacuum deposited gold layer.[34] We have observed a similar effect for the optical response of the FO gate electrodes upon potential application (see Figure S21, SI). The optical signal characteristics and sensitivity are almost unaffected, comparing them before and after potential applications, hence the sensing capabilities are not influenced
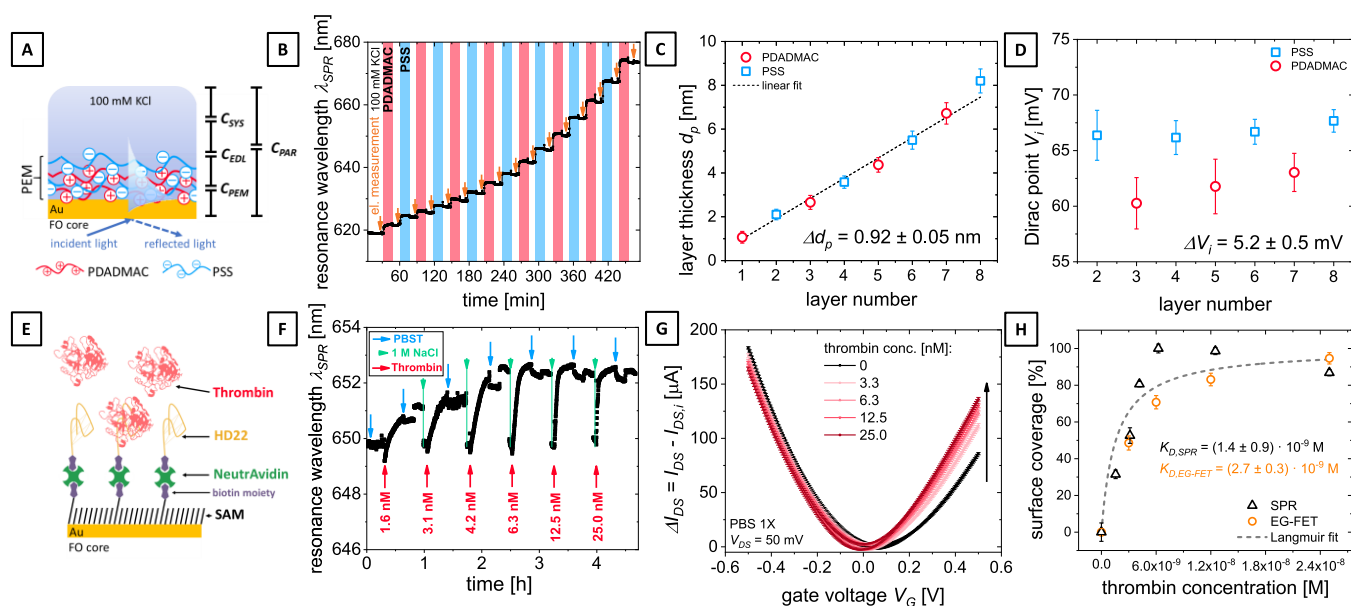
Figure 4. (A) Schematic representation of the layer assembly and the capacitive circuit on the right side. (B) SPR kinetics for 15 consecutive layers. (C) Thickness evaluated for the first eight layers from SPR data. (D) Dirac point evaluation from the $I_{DS}V_G$ curves of the EG-FET. (E) Schematic representation of the thrombin assay and (F) SPR titration curves for thrombin binding (red arrows). Washing steps are indicated by blue arrows and green arrows mark 1 M NaCl regeneration steps (cut from data). (G) $I_{DS}V_G$ curves for thrombin after binding at concentrations ranging from 3.3 to 25 nM. (H) Langmuir binding curves for EG-FET (orange data points) and SPR (black data points).

by the simultaneous use of the FO tips as gate electrodes. Furthermore, these effects are minimized if the Au surface is functionalized with, e.g., a self-assembly monolayer typically used in biosensing assays acting as a shielding layer for the Au surface.

In addition, the coupling intensity for different l_o values was investigated for further optimization of the optical signal (see Figure S18, SI). Therefore, the quality factor q of the device was evaluated by investigating the ratio of intensity to the full width at half-maximum (FWHM) of the SPR spectra with the variation of the effective SPR zone length (definition of q is shown in Section S7, SI). The results are shown in Figure 3D and lead to the conclusion that a SPR zone length l_o of 10 mm is best suited for FO probes with 1 mm d_{FO}. A high q factor results in lower noise of the optical signal which is based on tracking the minimum of the resonance dip in the reflected spectra. A representative optical signal obtained for such FO probe geometry is shown in the SI. Further signal characterization was performed using 2, 4, 6, 8, and 10% solutions of sucrose in DI-H$_2$O (Figures 3E and S19) and the obtained optical parameters (Section S7, SI) are in accordance with the current state of the art for this type of plasmonic FO setup.[36,37] Moreover, it has been shown that the sensitivity increases with the FO core diameter.[38] Figure 3F shows the dependency of the bulk sensitivity S_B on the core diameter, as determined from the sucrose calibration. Furthermore, the optimized l_o of 10 mm further increased γ to 10.4 and results in higher $I_{DS}V_G$ ratios (see Figure S20, SI). This trade-off made for an optimized FO gate electrode results in an optimal size regime of both devices.

To validate the sensor performance of the system, an LBL assembly of differently charged PEMs was monitored. Alternating layers of positively charged poly-(diallyldimethylammonium chloride) (PDADMAC) and negatively charged poly(sodium 4-styrenesulfonate) (PSS) were assembled on the FO gate electrode by dipping the FO gate

into the respective polymer solution (1 mg/mL in 0.1 M KCl) for 15 min with intermediate washing steps in 0.1 M KCl (Section S10, SI). Signal stability upon dipping the FO gate in external solutions prior to gate functionalization is shown in Figure S22. The layer growth on the FO gate was observed by continuous measurement of the optical response, confirming a parabolic trend of thickness increase with layer number (Figure 4B), as previously reported.[10] The layer thickness was derived from the resonance wavelength shift using a simulated calibration curve (see Figure S24, SI) and a refractive index n_p for the swollen PEM layers of 1.476.[39] The obtained PEM layer thickness for the linear region of the first eight layers is shown in Figure 4C. An average increase in layer thickness Δd_p of 0.92 ± 0.05 nm was obtained. The average surface mass density $\Delta\Gamma$ increase per layer was determined by the equation

$$\Delta\Gamma = \Delta d_p \cdot (n_p - n_s) \cdot \left(\frac{\partial n}{\partial c}\right)^{-1} \tag{3}$$

where $\partial n/\partial c$ is the coefficient relating the changes in the refractive index to the polymer concentration bound to the surface and was set to 0.2 mm^3/mg.[40] The resulting $\Delta\Gamma = 66 \pm 4$ ng/cm^2 is in excellent agreement with the previously reported findings using a planar Kretschmann-SPR based configuration.[10] Electronic characterization ($I_{DS}V_G$) was performed after each washing step and before functionalization with the new PEM layer by dipping the FO gate into the EG-FET reaction chamber in 0.1 M KCl. In agreement with previously reported findings, PDADMAC layers shift the $I_{DS}V_G$ curve to more negative V_G values, whereas PSS layers shift the curve to more positive V_G values (Figure S25, SI).[39,41] The observed Dirac point shifts ΔV_i, associated with the different type of charges of the PEM layers are shown in Figure 4D and were in the range of 5.2 ± 0.5 mV. Real-time current measurements after PEM layer formation are shown in Figure S26 and indicate the subsequent electrical stabilization of the PEM layer, to which the optical signal is not sensitive. The EG-

FET can be represented by a series of capacitors at the gate/electrolyte (gate capacitance C_g) and channel/electrolyte (channel capacitance C_{ch}), in which the smaller capacitance will dominate the sensor response. Hence, as shown above, a beneficial γ ratio was chosen to make the gate electrode act as the working electrode, responsible for electrical transduction via capacitive coupling.[42] (Bio)chemical modifications of the gate surface (like LbL formation) induce an ion-based electrical double layer (EDL) modulation, which shifts the capacitance of the system and hence couples to the measured I_{DS} which serves as the device readout. This coupling can depend on the applied V_G with variable magnitude, depending on the types of interactions (Coulombic/Faradaic) involved. For the shown example of PEM formation, calculations of the capacitive model shown in Figure 4A yield PEM layer capacitances C_{PEM} of around 1.2 $\mu F/cm^2$, C_{EDL} of 29 $\mu F/cm^2$, and a total C_{tot} of 2.1 $\mu F/cm^2$. Hence, the capacitance change due to LbL formation has the highest impact on C_{tot} and can be readout by the EG-FET with variations in I_{DS} currents of around 20 μA for a single PEM layer. These results correspond to the Dirac point shifts shown in Figure 4D. The PEM layers were modeled as planar capacitors, $C_{PEM} = \epsilon_0 \epsilon_r d_p^{-1}$, with the layer thickness d_p obtained from the SPR results. Hence, the system could be used to evaluate the electrical permittivity of the immobilized layers.

To further validate the sensor capabilities, the system was tested and benchmarked using the biological assay: thrombin binding to a surface-immobilized, biotinylated aptamer (HD22), bound on NeutrAvidin OEG-biotin SAMs. The assay structure is shown in Figure 4E and is similar to the assay previously reported by our group.[18,43] The surface functionalization was monitored via SPR and EG-FET and binding of each assay component was confirmed thereby. Obtained optical signals result in a surface mass density of 255 ± 40 and 47 ± 9 ng/cm^2 for NeutrAvidin and HD22, respectively (Section S11, SI). The ratio between NeutrAvidin and HD22 is 1.1, corresponding to about one bound aptamer per bound NeutrAvidin on the surface, and was therefore controlled by the density of the immobilized NeutrAvidin linker. This is in excellent agreement with previously reported findings obtained in planar Kretschmann-SPR-based configuration.[43] Thrombin titration in the medically relevant range (5−20 nM) on the aptamer functionalized FO gate was continuously monitored by SPR for concentrations ranging from 1.6 to 25 nM and the time-resolved curve is shown in Figure 4F. In the saturation regime of each concentration, an $I_{DS}V_G$ curve was recorded and the sensor surface was consecutively regenerated with a 1 M NaCl solution. For clarity of representation, the data were segmented and the peaks originating from the regeneration cut from the timeline (raw data in Figure S27, SI). The resulting $I_{DS}V_G$ curves for each concentration are shown in Figure 4G. A shift in the Dirac point is observed, but more interestingly the electron accumulation branch of the curve is shifted significantly with increasing concentration. The localized charges of thrombin binding to the surface immobilized aptamer have been demonstrated to cause a negative ζ potential,[44] displacing the EDL, favorable for positively charged ion species. Consequently, the surface charge on the transistor channel is adjusted to the EDL, modifying the EG-FET output via capacitive coupling more dominantly by changes in electron mobility. These shifts in I_{DS} were evaluated at V_G = 0.5 V against the titrated thrombin concentration and a Langmuir-type saturation is observed, with a binding affinity

constant of $K_D = (2.7 \pm 0.3) \times 10^{-9}$ M. Evaluation of the electronic signal at different gate voltages within the electron accumulation branch of the $I_{DS}V_G$ curve results in similar K_D values, validating the approach used for signal analysis (Figure S29). The resulting data, overlaid with the responses from the SPR, is shown in Figure 4H. The SPR response curve also shows Langmuir-type characteristics and evaluation of the binding affinity yields a $K_D = (1.4 \pm 0.9) \times 10^{-9}$ M. This is in good agreement for both sensor type systems and with the previous results reported in the literature.[43] We extrapolated the limit of detection (LoD) from the sensor response signals in the Langmuir curve where three time the standard deviation of the baseline level is intersected. For the optical signal the LoD was found below the 1 nM range with a satisfactory signal to noise ratio. By the same principle, for the EG-FET a LoD of 0.2 nM was found. The coupling of the two systems allows for the quantification of the measured current shifts. As shown in the SI it can be estimated that a shift of 25.7 μA, evaluated at V_G = 500 mV, corresponds to $(1.1 \pm 0.2) \times 10^{12}$ bound thrombin/cm^2. Other studies have shown that by the implementation of a sophisticated surface functionalization method, the capabilities of the capacitive sensing approach for EG-FETs can be further exploited, potentially leading to single molecule detection.[3]

CONCLUSIONS

A novel sensor system for multivariant surface binding investigations is presented. The platform allows for obtaining optical and electrical signals simultaneously, yielding complementary information about mass and charge uptake and redistribution on the FO gate surface. Drawbacks of the traditional SPR configuration that increase the sensor platform costs can be compensated by replacing the prism with an optical fiber. The optimized FO gate configuration also avoids the use of precise mounting systems leading to a flexible, compact, and even a portable sensor system. The advantages of the dual-sensing mode approach are shown by evaluating the charge and mass of components separately. The SPR yields precise information on the number of molecules bound to the surface. The EG-FET system verified the predominant binding configuration of thrombin to the aptamer by displacement of the electrical double layer leading to more pronounced shifts in the electron accumulation branch of the FET transfer characteristic. The coupling of the two systems allows controlled gate functionalization, confirmation of analyte binding, and quantification of the electronic response. Based on the results, we envision that this platform can not only provide new insights into bio-analyte interactions by detailed analysis of mass and charge contributions but can also lead to more robust and reliable biosensors.

ASSOCIATED CONTENT

ⓈI Supporting Information

The Supporting Information is available free of charge at https://pubs.acs.org/doi/10.1021/acssensors.1c02313.

> List of used chemicals, details of FET fabrication, setup, FO gate characterization (SEM, AFM), electrical characterization; optimized signals of FO probes; optical signal characterization; analysis of LBL assembly and thrombin binding assay (PDF)

■ AUTHOR INFORMATION

Corresponding Authors

Roger Hasler − *AIT Austrian Institute of Technology GmbH, 3430 Tulln, Austria;* orcid.org/0000-0002-0883-3053; Email: roger.hasler@ait.ac.at

Wolfgang Knoll − *AIT Austrian Institute of Technology GmbH, 3430 Tulln, Austria; Danube Private University, 3500 Krems an der Donau, Austria;* orcid.org/0000-0003-1543-4090; Email: wolfgang.knoll@ait.ac.at

Authors

Ciril Reiner-Rozman − *Danube Private University, 3500 Krems an der Donau, Austria*

Stefan Fossati − *AIT Austrian Institute of Technology GmbH, 3430 Tulln, Austria;* orcid.org/0000-0002-1109-0035

Patrik Aspermair − *AIT Austrian Institute of Technology GmbH, 3430 Tulln, Austria*

Jakub Dostalek − *AIT Austrian Institute of Technology GmbH, 3430 Tulln, Austria; FZU-Institute of Physics, Czech Academy of Sciences, Prague 182 21, Czech Republic;* orcid.org/0000-0002-0431-2170

Seungho Lee − *Institute of Science and Technology Austria, 3400 Klosterneuburg, Austria;* orcid.org/0000-0002-6962-8598

Maria Ibáñez − *Institute of Science and Technology Austria, 3400 Klosterneuburg, Austria;* orcid.org/0000-0001-5013-2843

Johannes Bintinger − *AIT Austrian Institute of Technology GmbH, 3430 Tulln, Austria; Danube Private University, 3500 Krems an der Donau, Austria;* orcid.org/0000-0002-6397-4254

Complete contact information is available at:
https://pubs.acs.org/10.1021/acssensors.1c02313

■ ACKNOWLEDGMENTS

■ REFERENCES

(1) Torricelli, F.; Adrahtas, D. Z.; Bao, Z.; Berggren, M.; Biscarini, F.; Bonfiglio, A.; Bortolotti, C. A.; Frisbie, C. D.; Macchia, E.; Malliaras, G. G.; McCulloch, I.; Moser, M.; Nguyen, T.-Q.; Owens, R. M.; Salleo, A.; Spanu, A.; Torsi, L. Electrolyte-Gated Transistors for Enhanced Performance Bioelectronics. *Nat. Rev. Methods Primers* **2021**, *1*, No. 66.

(2) Nakatsuka, N.; Yang, K.-A.; Abendroth, J. M.; Cheung, K. M.; Xu, X.; Yang, H.; Zhao, C.; Zhu, B.; Rim, Y. S.; Yang, Y.; et al. Aptamer−Field-Effect Transistors Overcome Debye Length Limitations for Small-Molecule Sensing. *Science* **2018**, *362*, 319−324.

(3) Macchia, E.; Manoli, K.; Holzer, B.; Di Franco, C.; Ghittorelli, M.; Torricelli, F.; Alberga, D.; Mangiatordi, G. F.; Palazzo, G.; Scamarcio, G.; et al. Single-Molecule Detection with a Millimetre-Sized Transistor. *Nat. Commun.* **2018**, *9*, No. 3223.

(4) Fahlman, M.; Fabiano, S.; Gueskine, V.; Simon, D.; Berggren, M.; Crispin, X. Interfaces in Organic Electronics. *Nat. Rev. Mater.* **2019**, *4*, 627−650.

(5) Goda, T.; Maeda, Y.; Miyahara, Y. Simultaneous Monitoring of Protein Adsorption Kinetics Using a Quartz Crystal Microbalance and Field-Effect Transistor Integrated Device. *Anal. Chem.* **2012**, *84*, 7308−7314.

(6) Okuda, S.; Ono, T.; Kanai, Y.; Ikuta, T.; Shimatani, M.; Ogawa, S.; Maehashi, K.; Inoue, K.; Matsumoto, K. Graphene Surface Acoustic Wave Sensor for Simultaneous Detection of Charge and Mass. *ACS Sens.* **2018**, *3*, 200−204.

(7) Zhang, Y.; Ding, Y.; Li, C.; Xu, H.; Liu, C.; Wang, J.; Ma, Y.; Ren, J.; Zhao, Y.; Yue, W. An Optic-Fiber Graphene Field Effect Transistor Biosensor for the Detection of Single-Stranded DNA. *Anal. Methods* **2021**, *13*, 1839−1846.

(8) Thomas, N.; Singh, V.; Kuss, S. Optical Fibers in Analytical Electrochemistry: Recent Developments in Probe Design and Applications. *TrAC, Trends Anal. Chem.* **2021**, No. 116196.

(9) Potyrailo, R. A. Multivariable Sensors for Ubiquitous Monitoring of Gases in the Era of Internet of Things and Industrial Internet. *Chem. Rev.* **2016**, *116*, 11877−11923.

(10) Aspermair, P.; Ramach, U.; Reiner-Rozman, C.; Fossati, S.; Lechner, B.; Moya, S. E.; Azzaroni, O.; Dostalek, J.; Szunerits, S.; Knoll, W.; Bintinger, J. Dual Monitoring of Surface Reactions in Real Time by Combined Surface-Plasmon Resonance and Field-Effect Transistor Interrogation. *J. Am. Chem. Soc.* **2020**, 11709.

(11) Sui, B.; Xu, Y.; Wang, Z.; Zhang, C.; Qin, L.; Li, X.; Wu, S. Simultaneously Performing Optical and Electrical Responses from a Plasmonic Sensor Based on Gold/Silicon Schottky Junction. *Opt. Express* **2019**, *27*, 38382.

(12) Wong, A. T.; Noh, J. H.; Pudasaini, P. R.; Wolf, B.; Balke, N.; Herklotz, A.; Sharma, Y.; Haglund, A. V.; Dai, S.; Mandrus, D.; et al. Impact of Gate Geometry on Ionic Liquid Gated Ionotronic Systems. *APL Mater.* **2017**, *5*, No. 042501.

(13) Kaur, B.; Sharma, A. K. Plasmonic Biosensor in NIR with Chalcogenide Glass Material: On the Role of Probe Geometry, Wavelength, and 2D Material. *Sens. Imaging* **2018**, *19*, No. 36.

(14) Gu, J.-E.; Lee, S.; Stafford, C. M.; Lee, J. S.; Choi, W.; Kim, B.-Y.; Baek, K.-Y.; Chan, E. P.; Chung, J. Y.; Bang, J.; Lee, J.-H. Molecular Layer-by-Layer Assembled Thin-Film Composite Membranes for Water Desalination. *Adv. Mater.* **2013**, *25*, 4778−4782.

(15) Ariga, K.; Lvov, Y. M.; Kawakami, K.; Ji, Q.; Hill, J. P. Layer-by-Layer Self-Assembled Shells for Drug Delivery. *Adv. Drug Delivery Rev.* **2011**, *63*, 762−771.

(16) Pollet, J.; Delport, F.; Janssen, K. P.; Jans, K.; Maes, G.; Pfeiffer, H.; Wevers, M.; Lammertyn, J. Fiber Optic SPR Biosensing of DNA Hybridization and DNA−Protein Interactions. *Biosens. Bioelectron.* **2009**, *25*, 864−869.

(17) Reiner-Rozman, C.; Hasler, R.; Andersson, J.; Rodrigues, T.; Bozdogan, A.; Bintinger, J.; Aspermair, P. The Top Performer: Towards Optimized Parameters for Reduced Graphene Oxide Uniformity by Spin Coating. *Micro Nano Lett.* **2021**, 436.

(18) Kotlarek, D.; Vorobii, M.; Ogieglo, W.; Knoll, W.; Rodriguez-Emmenegger, C.; Dostálek, J. Compact Grating-Coupled Biosensor for the Analysis of Thrombin. *ACS Sens.* **2019**, *4*, 2109−2116.

(19) Reiner, A. T.; Ferrer, N.-G.; Venugopalan, P.; Lai, R. C.; Lim, S. K.; Dostálek, J. Magnetic Nanoparticle-Enhanced Surface Plasmon Resonance Biosensor for Extracellular Vesicle Analysis. *Analyst* **2017**, *142*, 3913−3921.

(20) Reiner-Rozman, C.; Kotlowski, C.; Knoll, W. Electronic Biosensing with Functionalized RGO FETs. *Biosensors* **2016**, *6*, No. 17.

(21) Torsi, L.; Magliulo, M.; Manoli, K.; Palazzo, G. Organic Field-Effect Transistor Sensors: A Tutorial Review. *Chem. Soc. Rev.* **2013**, *42*, 8612−8628.

(22) Homola, J.; Yee, S. S.; Gauglitz, G. Surface Plasmon Resonance Sensors. *Sens. Actuators, B* **1999**, *54*, 3−15.

(23) Jorgenson, R. C.; Yee, S. S. A Fiber-Optic Chemical Sensor Based on Surface Plasmon Resonance. *Sens. Actuators, B* **1993**, *12*, 213−220.

(24) Xu, Y.; Jones, N. B.; Fothergill, J. C.; Hanning, C. D. Analytical Estimates of the Characteristics of Surface Plasmon Resonance Fibre-Optic Sensors. *J. Mod. Opt.* **2000**, *47*, 1099−1110.

(25) Cicoira, F.; Sessolo, M.; Yaghmazadeh, O.; DeFranco, J. A.; Yang, S. Y.; Malliaras, G. G. Influence of Device Geometry on Sensor Characteristics of Planar Organic Electrochemical Transistors. *Adv. Mater.* **2010**, *22*, 1012−1016.

(26) O'Suilleabhain, D.; Kelly, A. G.; Tian, R.; Gabbett, C.; Horvath, D.; Coleman, J. N. Effect of the Gate Volume on the Performance of Printed Nanosheet Network-Based Transistors. *ACS Appl. Electron. Mater.* **2020**, *2*, 2164−2170.

(27) Delavari, N.; Tybrandt, K.; Berggren, M.; Piro, B.; Noël, V.; Mattana, G.; Zozoulenko, I. Nernst−Planck−Poisson Analysis of Electrolyte-Gated Organic Field-Effect Transistors. *Phys. D: Appl. Phys.* **2021**, *54*, No. 415101.

(28) Abràmoff, M. D.; Magalhães, P. J.; Ram, S. J. Image Processing with ImageJ. *Biophotonics Int.* **2004**, *11*, 36−42.

(29) Smits, E. C.; Anthopoulos, T. D.; Setayesh, S.; Van Veenendaal, E.; Coehoorn, R.; Blom, P. W.; De Boer, B.; De Leeuw, D. M. Ambipolar Charge Transport in Organic Field-Effect Transistors. *Phys. Rev. B* **2006**, *73*, No. 205316.

(30) Lin, J.-H.; Liu, Y.; Zhang, Q. Influence of the Electrolyte Film Thickness on Charge Dynamics of Ionic Liquids in Ionic Electroactive Devices. *Macromolecules* **2012**, *45*, 2050−2056.

(31) Hyun, W. J.; Bidoky, F. Z.; Walker, S. B.; Lewis, J. A.; Francis, L. F.; Frisbie, C. D. Printed, Self-Aligned Side-Gate Organic Transistors with a Sub-5 Mm Gate−Channel Distance on Imprinted Plastic Substrates. *Adv. Electron. Mater.* **2016**, *2*, No. 1600293.

(32) Mello, H.; Dalgleish, S.; Ligorio, G.; Mulato, M.; List-Kratchvil, E. In *Stability Evaluation and Gate-Distance Effects on Electrolyte-Gated Organic Field-Effect Transistor Based on Organic Semiconductors*, Organic and Hybrid Sensors and Bioelectronics XI; International Society for Optics and Photonics, 2018; Vol. *10738*, p 1073819.

(33) McIntyre, J. Electrochemical Modulation Spectroscopy. *Surf. Sci.* **1973**, *37*, 658−682.

(34) Dahlin, A. B.; Zahn, R.; Vörös, J. Nanoplasmonic Sensing of Metal−Halide Complex Formation and the Electric Double Layer Capacitor. *Nanoscale* **2012**, *4*, 2339−2351.

(35) Dahlin, A. B.; Sannomiya, T.; Zahn, R.; Sotiriou, G. A.; Vörös, J. Electrochemical Crystallization of Plasmonic Nanostructures. *Nano Lett.* **2011**, *11*, 1337−1343.

(36) Socorro-Leránoz, A. B.; Santano, D.; Del Villar, I.; Matias, I. Trends in the Design of Wavelength-Based Optical Fibre Biosensors (2008−2018). *Biosens. Bioelectron.: X* **2019**, *1*, No. 100015.

(37) Arghir, I.; Delport, F.; Spasic, D.; Lammertyn, J. Smart Design of Fiber Optic Surfaces for Improved Plasmonic Biosensing. *New Biotechnol.* **2015**, *32*, 473−484.

(38) Dwivedi, Y. S.; Sharma, A. K.; Gupta, B. D. Influence of Skew Rays on the Sensitivity and Signal-to-Noise Ratio of a Fiber-Optic Surface-Plasmon-Resonance Sensor: A Theoretical Study. *Appl. Opt.* **2007**, *46*, 4563−4569.

(39) Piccinini, E.; Alberti, S.; Longo, G. S.; Berninger, T.; Breu, J.; Dostalek, J.; Azzaroni, O.; Knoll, W. Pushing the Boundaries of Interfacial Sensitivity in Graphene FET Sensors: Polyelectrolyte Multilayers Strongly Increase the Debye Screening Length. *J. Phys. Chem. C* **2018**, *122*, 10181−10188.

(40) Perlmann, G. E.; Longsworth, L. G. The Specific Refractive Increment of Some Purified Proteins. *J. Am. Chem. Soc.* **1948**, *70*, 2719−2724.

(41) Wang, Y. Y.; Burke, P. J. Polyelectrolyte Multilayer Electrostatic Gating of Graphene Field-Effect Transistors. *Nano Res.* **2014**, *7*, 1650−1658.

(42) Manoli, K.; Magliulo, M.; Mulla, M. Y.; Singh, M.; Sabbatini, L.; Palazzo, G.; Torsi, L. Printable Bioelectronics to Investigate Functional Biological Interfaces. *Angew. Chem., Int. Ed.* **2015**, *54*, 12562−12576.

(43) Kotlarek, D.; Curti, F.; Vorobii, M.; Corradini, R.; Careri, M.; Knoll, W.; Rodriguez-Emmenegger, C.; Dostálek, J. Surface Plasmon Resonance-Based Aptasensor for Direct Monitoring of Thrombin in a Minimally Processed Human Blood. *Sens. Actuators, B* **2020**, *320*, No. 128380.

(44) Tan, S. Y.; Acquah, C.; Tan, S. Y.; Ongkudon, C. M.; Danquah, M. K. Characterisation of Charge Distribution and Stability of Aptamer-Thrombin Binding Interaction. *Process Biochem.* **2017**, *60*, 42−51.